

Thickness dependent growth of Ge nanoparticles in amorphous Ge/SiO₂ multilayers

B. Pivac^{a,*}, P. Dubček^a, H. Zorc^a, S. Bernstorff^b, B. Vlahovic^c, J. Zavašnik^d

^a Ruder Bošković Institute, Bijenička 54, 10000, Zagreb, Croatia

^b Elettra-Sincrotrone Trieste, SS 14, Km 163.5, 34149, Basovizza, TS, Italy

^c North Carolina Central University, 27707, Durham, NC, USA

^d Jožef Stefan Institute, Jamova Cesta 39, 1000, Ljubljana, Slovenia

ARTICLE INFO

Keywords:

Ge nanoparticles
AFM
SEM
TEM
GISAXS
Raman spectroscopy

ABSTRACT

Amorphous Ge/SiO₂ multilayers were deposited in a high vacuum by an e-gun assisted physical vapor deposition technique with continuous Ge layers either 2 or 4 nm thick, separated by 2 nm thick SiO₂ layers. The aim was to explore whether annealing of these multilayers at a rather low temperature will produce Ge nanoparticles suitable for solar cell applications. All samples were characterized by scanning electron microscopy (SEM), atomic force microscopy (AFM), transmission electron microscopy (TEM) in cross-section, grazing incidence X-ray diffraction, Raman spectroscopy and grazing incidence small-angle X-ray scattering (GISAXS). It is found that annealing of very thin continuous amorphous Ge layers will lead to mostly spherical crystalline nanoparticles (NPs) of the desired size. On the other hand, from thicker Ge layers, a bimodal distribution is obtained consisting of smaller sphere-like and larger oblate spheroids, as confirmed by a calculated simulation.

1. Introduction

The properties of nanosized semiconductor crystals (often generally called quantum dots) have attracted significant attention as their properties strictly depend on their size and shape. When the dimension of such objects reaches nanometric size quantum confinement becomes important and is dominating the material properties. More specifically the optical band gap and the efficiency of indirect optical transitions are increased [1,2]. Hence such nanoparticles demonstrate optical tunability and enhanced efficiency in interacting with light.

Silicon nanoparticles (NPs) incorporated into dielectrics were intensively studied lately due to their compatibility with modern semiconductor technology [3]. It was shown that the variation in the Si NPs optical bandgap depends not only on the size and shape of the NPs but also on the deposition technique and/or amorphous/crystalline phase of the NPs [4].

Lately, however, Ge NPs are receiving a larger attention for photovoltaic (PV) applications due to the lower processing temperature and the larger excitonic Bohr radius (about 20 nm). It was shown that Ge NPs, when produced in sizes of 1–3 nm, exhibit a high tunability of the band gap with a shift of the conduction band from 0.2 to 1.1 eV [5]. Aiming to obtain similar small Ge NPs we have explored their formation

in amorphous SiO₂/Ge multilayers deposited by physical vapor deposition (PVD) with an e-gun as a fast, simple and reliable method [6,7], where the thickness of the deposited Ge layers was 2 or 4 nm. The Ge crystallization in very thin amorphous layers has been explored [8–10] and while some reports found that Ge does not crystallize in very thin (2 nm) layers [9,10], other reports [11,12] found Ge crystallization already in 1 nm thick films with relatively large isolated fibrous grains.

The main purpose of this work is to further explore the onset of crystallization of Ge NPs, their size and shape when clustered from continuous amorphous Ge layers of different thicknesses, deposited between insulating amorphous SiO₂ layers forming superstructures suitable for photovoltaic applications. Besides targeting the size of the formed NPs to be in the range 1–3 nm, we wanted to explore whether the starting thickness of the Ge layer will determine and/or affect the size of the NPs.

2. Experimental procedure

Multilayers consisting of 20 bilayers of alternating amorphous SiO₂ (2 nm thick) and Ge layers, where each Ge layer was either 2 nm or 4 nm thick, starting with a SiO₂ layer, were prepared by e-gun assisted deposition in vacuum of about 5 · 10⁻⁴ Pa. The details of the samples

* Corresponding author.

E-mail address: pivac@irb.hr (B. Pivac).

<https://doi.org/10.1016/j.vacuum.2021.110294>

Received 31 December 2020; Received in revised form 30 April 2021; Accepted 4 May 2021

Available online 17 May 2021

0042-207X/© 2021 Elsevier Ltd. All rights reserved.

preparation and annealing are given in Ref. [7]. Standard Si (100) wafers with a diameter of 100 mm were used as substrates. Prior to deposition the substrates were cleaned using trichloroethylene and methanol in an ultrasonic bath. After cleaning the substrates were etched in buffered HF to remove native SiO₂ from the surface, than rinsed in deionized water and blown dry with spectroscopic pure N₂ gas. The film thickness during growth was measured with a calibrated quartz balance.

A schematic presentation of samples as-deposited and after annealing above 500 °C are shown in Fig. 1. The Sample coding is given in Table 1.

The morphology and chemistry of the deposited thin films were analyzed by scanning electron microscopy (SEM; Prisma-E, Thermo Fisher Scientific). Samples were mounted onto Al support stubs by silver adhesive paint at 45° to expose the stacking sequence (Fig. 2). As the samples are conductive enough, they were not further coated or modified.

The details of the surface structures and morphology were analyzed by atomic force microscopy (AFM; Nova 1138, NT-MDT) in the semi-contact mode; the recorded data were interpreted by the Nova 1.0.26 RC1 software.

The crystallinity and phase composition of the samples were analyzed by cross-section transmission electron microscopy (X-TEM, JEM-2100, Jeol Inc.), operating at 200 kV; all the micrographs were recorded by a slow-scan CCD camera (Orius SC-1000, Gatan). The samples were prepared in cross-section, mechanically thinned and etched by Ar⁺ ions as described in Ref. [13].

The overall crystallinity characteristics were obtained from Grazing incidence X-ray diffraction (GIXRD). The data were collected with a Siemens D5000 X-ray diffractometer equipped with a Goebel mirror which filtered and collimated the incident beam. A Soller filter was placed in front of the scintillation detector. The radiation source was a copper X-ray tube (Cu K_{α1} radiation, $\lambda = 1.54 \text{ \AA}$). The selected grazing incident angle was 0.3°, and the 2 θ range from 20° to 65° was recorded.

The details of the NPs morphology were studied by Grazing incidence small-angle X-ray scattering (GISAXS) measurements which were performed at Elettra-Sincrotrone, Trieste, Italy, on the Austrian SAXS beamline [14], using synchrotron radiation with wavelength $\lambda = 0.154 \text{ nm}$ (photon energy of 8 keV).

The crystallization monitoring was further supported by Raman spectroscopy. All Raman spectra were acquired at room temperature in back-scattering geometry on a Labram HR Evolution system equipped with a microscope (magnification 100 X) and a 473 nm laser excitation source. The details of the GISAXS and Raman spectroscopy analysis are also presented in Ref. [7].

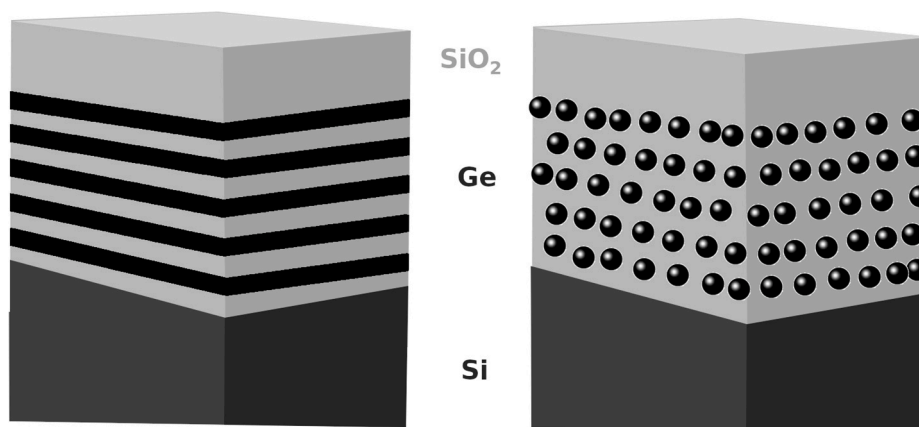


Fig. 1. Schematic representation of multilayers consisting of alternative layers of 2 nm SiO₂ (grey) and 2 or 4 nm Ge (black) with a 20 nm thick SiO₂ capping layer at the top: as-deposited (left), and after annealing above 500 °C (right).

Table 1
Samples coding.

Sample	As deposited	Annealed @525 °C	Annealed @550 °C
SiO ₂ (2 nm)/Ge(2 nm) [20 bilayers]	A1	A2	
SiO ₂ (2 nm)/Ge(4 nm) [20 bilayers]	B1		B2

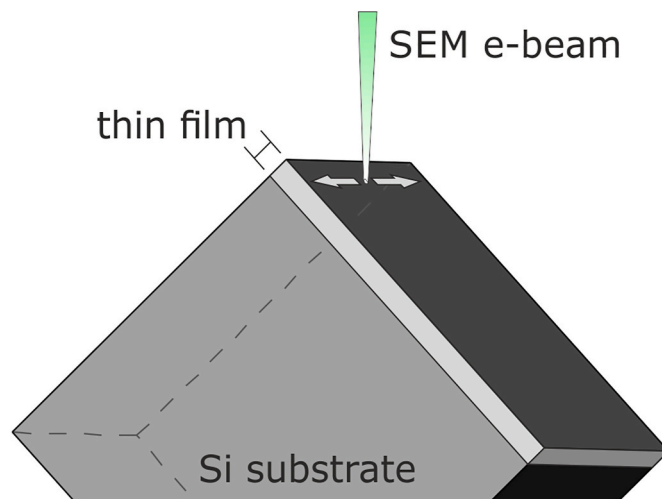


Fig. 2. The schematic (sketch) of sample mounting for scanning electron microscopy; the sample is tilted by 45° for surface morphology and composition analysis.

3. Results and discussion

3.1. Surface, microstructure, and phase composition characterization of the samples

The analysis of the as-deposited and annealed samples are collected in a Tableau (Fig. 3). The scanning electron microscopy (SEM) images of the as-deposited thin film samples A1 and B1 show the variation of the secondary electrons (SE) contrast due to surface roughness. On the other hand, the backscattered electrons (BE) contrast is uniform, and no agglomerations or precipitates were formed after deposition. After annealing, the SE contrast is more uniform and the surface appears smoother. Moreover, the BE contrast remained the same before and after annealing. To further explore the surface morphology alterations, the

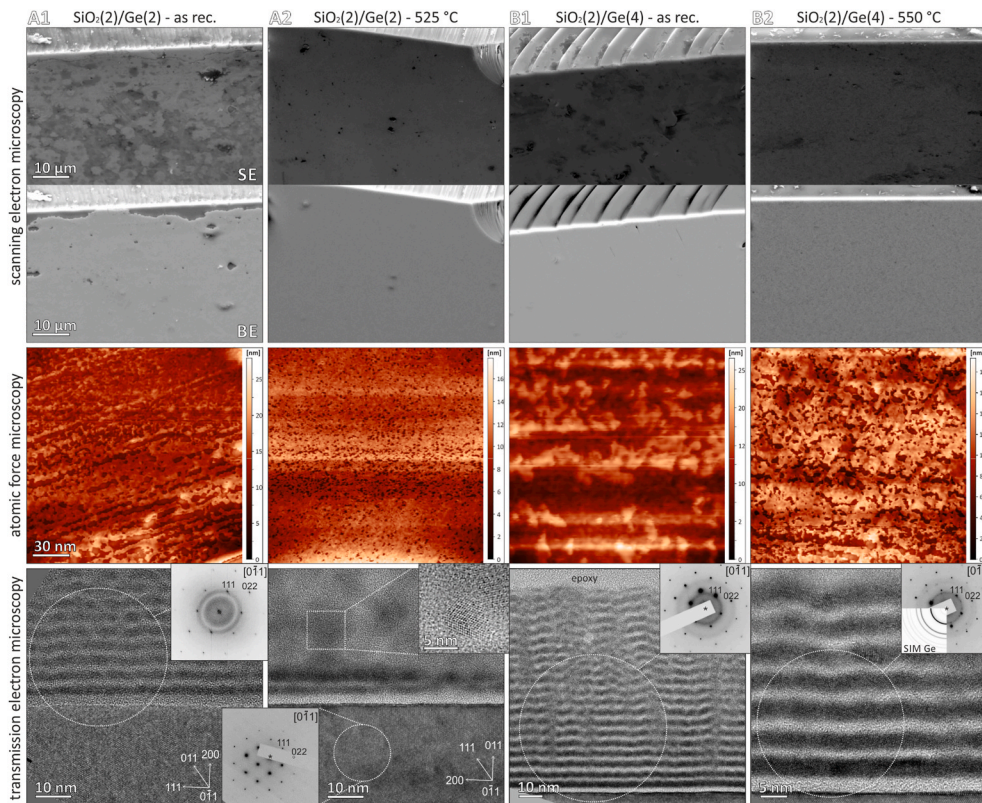


Fig. 3. The hierarchical characterization of the as-deposited (A1, B1) and annealed samples (A2, B2), deposited on single-crystal Si substrate. The 1st and 2nd line present SEM SE and BE micrographs of the thin films, observed at 45° tilt angle (all images were recorded at the same conditions and magnification). The following line presents AFM images of the sample's surface (scan size of $2 \times 2 \mu\text{m}$), showing smoothing of the surface after annealing (A2, B2). The bottom line shows X-TEM micrographs with corresponding SAED diffractions of completely amorphous (A1, B1) and crystalline Ge and amorphous SiO_2 layers (A2, B2). All SAED were recorded to include the Si substrate (indexed in SAED).

samples were investigated by atomic force microscopy (AFM). The as-deposited samples have a surface roughness of about 25 nm, which is, after annealing, reduced down to 16 nm.

The internal structure of the as-deposited and annealed multilayer thin films was analyzed by cross-sectional transmission electron microscopy (X-TEM). In both as-deposited samples (A1 and B1), we can observe the deposited 20 bilayers of alternating SiO_2 and Ge amorphous layers, the latter with nominal thickness of 2 nm for sample A1 and 4 nm for sample B1. As both the SiO_2 and Ge phases are amorphous, as confirmed by the selected area electron diffraction pattern (SAED), the contrast in the TEM micrographs originates solely from the mass-thickness contrast and the alterations of brighter SiO_2 and darker Ge layers are easily distinguishable. After annealing, the SiO_2 layers remain amorphous, while Ge forms nano-sized crystallites. The interpretation of such TEM micrographs is not so intuitive anymore, as with the crystalline phase, the diffraction contrast is now prevailing. The Ge nano-crystallites are randomly oriented, as confirmed by selected area electron diffraction experiments forming a characteristic ring-diffraction pattern. As the diffraction contrast depends on the orientation of the crystallites, on the TEM micrographs of the annealed samples (A2, B2), the lattice separation in crystallites will be visible only for the suitable-oriented Ge crystallites. Nevertheless, from HR-TEM (phase-contrast) observations, we can observe Ge NPs in the position of the former amorphous Ge layers, with an average size for the Ge NPs < 5 nm. As determined from selected area electron diffraction (SAED) experiments (shown in the insets of the TEM images), no intermediate Si–Ge phases were formed.

3.2. GIXRD analysis

All as-deposited and annealed samples were then analyzed by GIXRD measurements and the obtained diffraction pattern are shown in Fig. 4. All as-deposited samples, both with the deposited Ge layer thicknesses of 2 or 4 nm, produced two broad peaks characteristic for amorphous Ge.

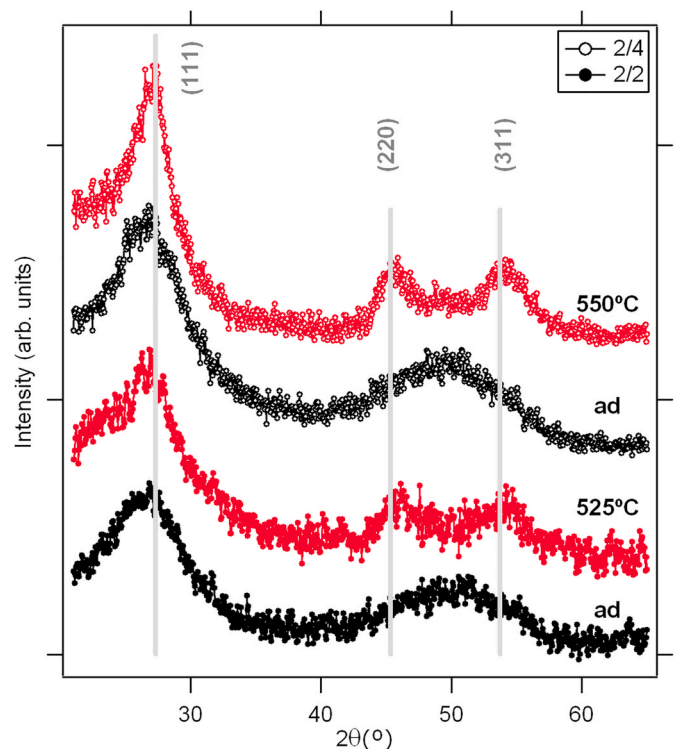


Fig. 4. GIXRD patterns of as-deposited (ad, black) and annealed at 525 °C and 550 °C (red) multilayers. The lower two curves are from the A samples and the upper two from the B samples. The curves are shifted in vertical direction for clarity. The vertical grey lines indicate the crystalline (111), (220) and (311) Ge peak positions.

The peaks centered at $2\theta \sim 26^\circ$ and $\sim 50^\circ$, correspond to the (111) and the partly overlapping (220) and (311) crystalline Ge peak positions, as they are not well resolved in the amorphous structure. The broad diffraction peak around 22° , present as a shoulder of the Ge (111) peak, belongs to the amorphous SiO_2 layer [15], which will be numerically deduced in the further analysis.

Annealing at 525°C (sample A2) and at 550°C (sample B2)), induced Ge clustering into nanocrystals, as evidenced by the appearance of the well-resolved (111), (220) and (311) crystalline Ge peaks. From the half-width of those peaks the crystallite sizes were determined by applying the Scherrer formula:

$$D = \frac{K\lambda}{B \cos \theta}$$

where λ is the applied X-ray wavelength, θ is the Bragg angle, B is the full width of the Bragg peak at half-maximum and K is a constant close to $K \sim 0.9$ within a few percent [16].

The values of the crystal domain size obtained from the GIWAXS measurements were $D = 2.0 \pm 0.1$ nm, $D = 2.0 \pm 0.1$ nm and $D = 2.2 \pm 0.1$ nm for the (111), (220) and (311) directions, respectively for the A2 sample, while the sample B2 shows at the onset of crystallization (550°C) the values $D = 2.6 \pm 0.1$ nm, $D = 3.7 \pm 0.1$ nm and $D = 3.0 \pm 0.1$ nm for the (111), (220) and (311) directions, respectively.

From this, we conclude that the shape of the grown crystalline NPs was very close to the spherical one for the A2 sample annealed at 525°C . In addition, a fit of the (220) and (311) peaks (not shown in the figure) reveals the existence of an additional amorphous contribution to the Ge NPs. Furthermore, when the starting Ge layer was 4 nm thick, the NPs are having a less spherical shape (oblate) with an average size of about 3 nm (sample B2).

Also in both cases a significant portion of the Ge domains remained amorphous. From the integral intensity of the relevant peaks in the diffraction curves we estimated that in both cases the ratio of the crystalline to the amorphous part was about 50:50%.

3.3. GISAXS analysis

To gain a more complete picture of the Ge NPs precipitation as a function of the thickness of the deposited continuous amorphous Ge layers a GISAXS analysis was performed and the results are shown in Fig. 5. Starting from early experiments [17], GISAXS has recently developed into a very powerful method to explore the morphology and distribution of either islands on the surface or buried particles or even voids [18] in a matrix or in thin films, as in our case [19]. Moreover, due to the grazing incidence geometry applied here, the data are collected and averaged from a large area (up to a square centimeter) providing a reliable statistic information on the studied subject.

In Fig. 5. 3D GISAXS patterns are presented for as-deposited (right row) and annealed (left row) SiO_2/Ge multilayers A (rear) and B (front), respectively. For a better perspective, in addition to the q_y and q_z axes, a third axis showing the signal intensity is presented.

Since the main contribution to the SAXS signal derives from the surface roughness, masking therefore the signal emanating from the layered structure [20], we subtracted the GISAXS pattern obtained at the critical angle for grazing incidence $\alpha = \alpha_c$. Therefore, the differential intensity pattern presented in Fig. 5 displays only the information deriving from the volume of the multilayers. The as deposited A1 sample consisting of well-defined layers each 2 nm thick, presented a pronounced Bragg sheet (indicated by a green arrow in Fig. 5) [21] at about $q_z = 1.5 \text{ nm}^{-1}$. From the exact position of this peak (as shown in the inset of Fig. 6), a bilayer SiO_2/Ge thickness d can be calculated from the expression $d = 2\pi/q_z$, where q_z is the distance to the maximum of the first Bragg sheet. The average value obtained for the A1 sample is $d = 4.2$ nm, which is very close to the intended bilayer thickness during deposition [7]. While the same value for the B1 sample is $d = 5.8$ nm, which is also in very good agreement with the intended values (in this case also a second Bragg peak is visible in the effective range of the detector). Since the roughness contribution from the sample surface to the total signal was numerically removed, the remaining signal intensity at the position $q_y = 0$ is very low, suggesting the interface roughness

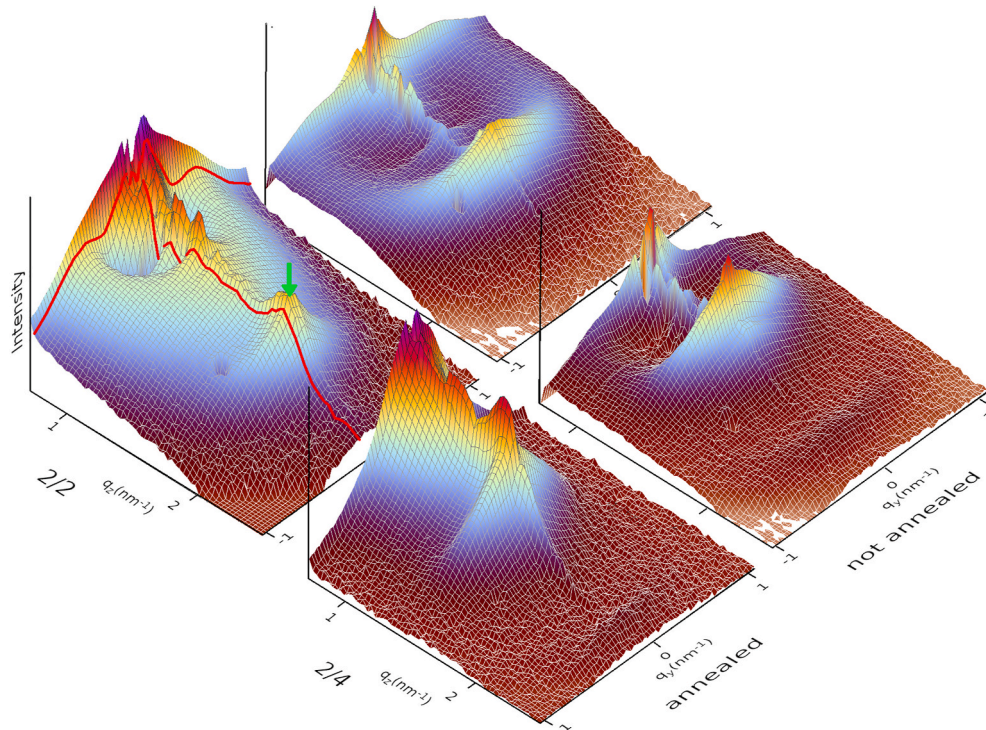


Fig. 5. 3D GISAXS patterns for B (front row), A (rear) samples before and after annealing at 550°C and 525°C . The red line parallel to the q_z axis indicates the position where the 1D cuts (presented in Fig. 6) were taken, and the red line parallel to the q_y axis shows the Yoneda plane.

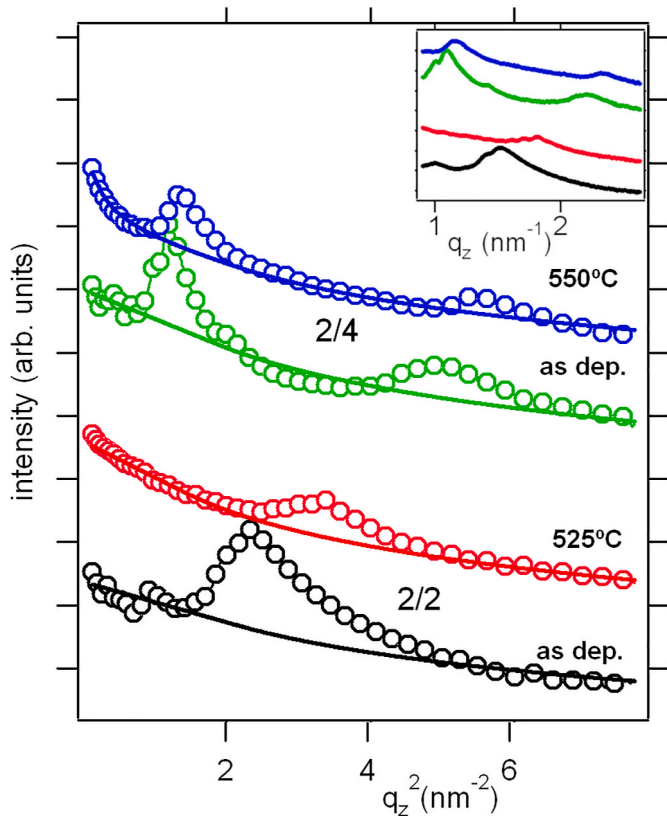


Fig. 6. GISAXS intensity taken along the q_z lines in Fig. 5 at $q_x = 0.12 \text{ nm}^{-1}$. The lower two curves present the A samples (as-deposited and annealed) and the upper two the B samples (both as-deposited and annealed). The full lines are the best fits for the size determination. The inset in the figure shows the intensity I vs. q used for the precise Bragg sheet value determination.

between different layers is not dominant, i.e. that the layers have quite smooth borders.

After annealing at 525 °C and 550 °C for 1 h for the A2 and B2 samples respectively, the Bragg sheets remained indicating the preservation of the well-ordered layers. The positions of the Bragg sheets are shifted to higher q values in both cases (clearly presented in the inset of Fig. 6), indicating as thickness of the bilayers $d = 3.5 \text{ nm}$ for the A2 and $d = 5.4 \text{ nm}$ for the B2 samples. The relative contraction of the layers, expressed as $(d_0 - d_a)/d_0$, is about 18% for the A2 sample and only about 6% for the B2 sample, suggesting that the contraction occurs dominantly in compacting the SiO_2 layer.

On the other hand, after annealing in both cases the signal close to the specular reflectance plane, i.e. close to $q_y = 0$ is significantly enhanced, suggesting an increase in the interface roughness with annealing. Qualitatively, it appears that the layer roughness of the interfaces in the B2 sample increases during annealing more than in the A2 case.

In Fig. 6 are shown linear cuts from Fig. 5 along the q_z direction (taken at $q_y = 0.12 \text{ nm}^{-1}$), showing the GISAXS intensity $I(q)$, where $q = 4\pi/\lambda \sin\theta$, λ is the wavelength of the applied X-ray radiation and 2θ is the scattering angle. In the Guinier approximation the intensity is related to the radius of gyration by the expression: $I(q) = I_0 \exp(-q^2 R_g^2/3)$, where I_0 is the incident intensity. This holds while $qR_g < 1$, approximately, and the dependence of $\ln(I)$ vs. q^2 (Guinier plot) should be linear. When different sizes are present, the plot would have slopes for appropriate angular ranges. The intensity for wider angles where $qR_g > 1$ decays as $I(q) = I_0 q^{-4}$ (Porod tail). We therefore used both types of dependence [22]:

$$I(q) = \begin{cases} G \exp\left(\frac{-q^2 R_g^2}{3}\right) & \text{for } q < q_1 \\ \frac{P}{q^\gamma} & \text{for } q > q_1 \end{cases}$$

here q is the scattering wave vector, R_g is the Guinier radius, γ is the Porod exponent and G and P are the Guinier and Porod scales, respectively. The point of switching from one to the other type of dependence (q_1) was chosen under the condition that the intensity remains a smooth function of the angle, i.e. the intensity and derivation of the intensity are equal for both dependencies at q_1 . This way the fits in Fig. 6 are no longer linear, but we can see that the scattering for $q^2 > 4 \text{ nm}^{-2}$ is caused by some additional and smaller particles.

From the fits shown by the full lines in Fig. 6, the values for R_g are calculated and given in Table 2. The values for the as-deposited sample A1 are very close, i.e. 1.5 and 1.3 for the vertical (out of plane) and horizontal (in plane) direction respectively, suggesting that the particles can be well approximated with spheres. In such case the real value of the sphere radius R can be obtained from the radius of gyration through the relation $R = \sqrt{\frac{3}{5}} R_g$, and it is in the range 1.6–1.9 nm. Similarly, in the as-deposited B1 sample, the existing NPs had a sphere radius in the range 2–2.3 nm. After annealing two sets of NPs developed. One smaller spherical with the radius $R = 2.2 \text{ nm}$ and another bigger described by an oblate spheroid with a smaller vertical axis of 2.3 nm and a bigger horizontal axis of 6.2 nm.

In Fig. 7 different Guinier plots ($\ln I$ versus q^2) are displayed, this time for the intensities along the horizontal direction. Dotted lines show the surface scattering contribution, which is significant only at very small q_y values for the not annealed samples.

The dashed lines show the combined contribution of the Guinier and Porod type of scattering, while the full lines show the sum. Due to the lateral correlation, the scattered intensity for both not annealed samples is depleted at small q_y values. This was accounted for in the model calculus as a structure factor given by the locally monodisperse approximation [23].

On the left side of Fig. 7 the fit is applied using only the Guinier contribution. We can see that the intensity can be fitted well only in the vicinity of the zero angle, while for $q_y > 2 \text{ nm}^{-2}$ one cannot tell if there is an additional contribution from smaller particles. On the right side, where the Porod tail was also calculated in, we see that the single particle size contribution obtained a very good fit for the A samples. This does not hold for the B annealed sample where two sizes of particles had to be calculated in order to get a good fit. From the sizes and relative intensity contribution we can estimate that the number of large particles is five times bigger than the small ones. All the obtained values for Guinier radii and Porod exponents are given in Table 2.

Given the deviation from the Porod law, we checked the nature of the Ge nanoparticles surface. Namely, we can look into the details of the deviation from the -4 exponent. First we normalized the intensity by the Q invariant, which is given by

$$Q = \int_0^\infty q^2 I(q) dq$$

where q is the scattering wave vector, and $I(q)$ is the measured intensity

Table 2

The in-plane correlation length ξ , the Hurst parameter, the calculated values for the vertical and horizontal radius of gyration R_{gv} and R_{gh} , and the Porod coefficient for the samples A and B, as-deposited and annealed.

Sample	ξ	Hurst	R_{gv}	R_{gh}	Porodcoeff.
A1	7.1	0.44	1.5	1.3	3.2
A2	7.0	0.24	2	2.8	3.6
B1	12.5	0.52	1.8	1.6	3.2
B2	13.1	0.32	1.7	4.8	3.6

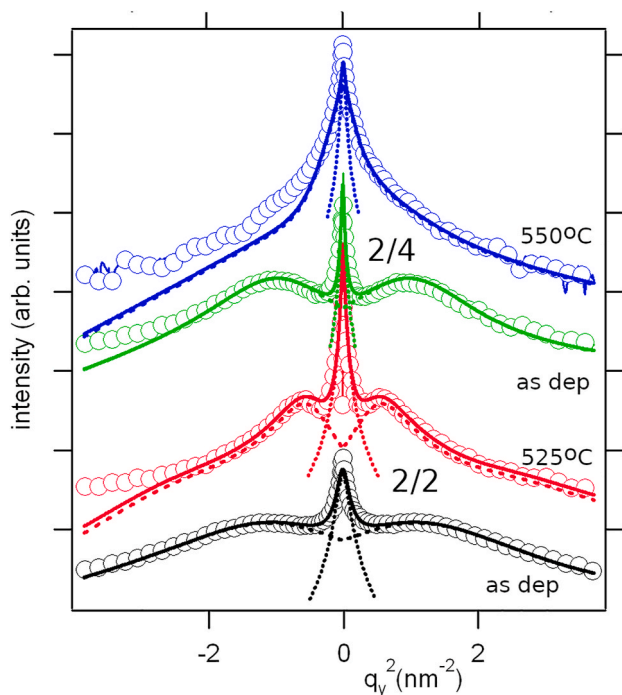


Fig. 7. 1D GISAXS intensity cuts taken parallel to each sample surface along the Yoneda maximum (see red line parallel to the q_y axis shown in Fig. 5).

which has been extrapolated to zero angle using $I(q) = I_0 \exp(-q^2 R_s^2/3)$, and to infinity using $I(q) = I_1 q^{-4}$. After plotting $\ln [q^4 I(q)]$ vs. q^2 (see Fig. 8) we observed a linear form of the wide angle part of the plot. Since the line has a positive coefficient, we estimated the size of the local density variations. These are 0.30 nm for both as deposited samples, increasing to 0.4 nm and 0.3 nm for the A2 and B2 samples, respectively.

The change in the layer-to-layer correlation can give us additional information about the nanoparticle formation [24,25]. Therefore, we investigated the horizontal (in plain) profiles of the first Bragg peaks that are shown in Fig. 9. The profiles were obtained by integration of the intensities in the narrow vertical range $\Delta q_z = \pm 0.05 \text{ nm}^{-1}$ and plotted

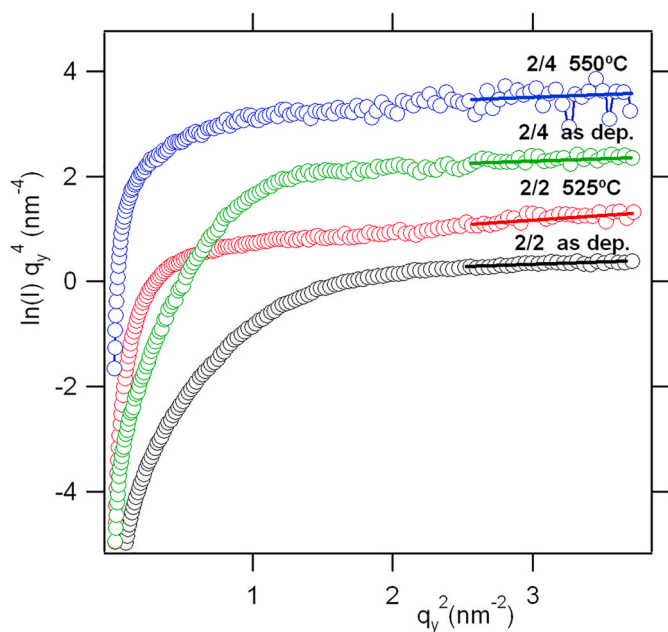


Fig. 8. Plot of $\ln [q^4 I(q)]$ vs. q^2 (open circles) and the best linear fit (full lines) for the large q range.

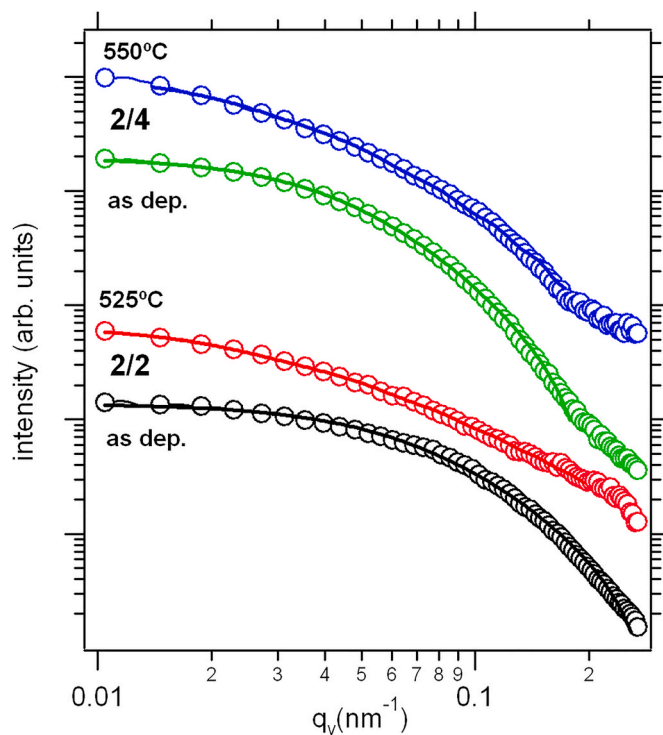


Fig. 9. Intensity profiles of the first Bragg peak in horizontal direction (open symbols) and the corresponding fits (full lines).

versus q_y . For a rough surface the height-to-height correlation can be modeled by ξ [26].

$$C(r) = \sigma^2 \exp\left[-(r/\xi)^{2H}\right]$$

where σ is the surface roughness, ξ is the in-plane correlation length, while the Hurst parameter H describes the quality („jaggedness“) of the surface: for an extremely jagged surface H approaches 0, while it is close to 1 for a very smooth surface. The intensity of the Bragg peak in horizontal direction is calculated as Fourier transform of the layer-to-layer correlation of this type, which is a good approximation when the surface roughness is small $q_z \sigma \ll 1$. The obtained values are listed in Table 2. It is interesting to note that the correlation length was not influenced significantly by the annealing, although the values are different for different Ge thickness: about 7 nm and 13 nm for the A2 and B2 samples. On the other hand, the Hurst parameter H was almost halved after the annealing for both kinds of sample, and it was about 0.5 for the as deposited samples. Already the initial as-deposited interface between Ge and SiO_2 was not smooth, which obviously deteriorated after the particle formation.

To further support the results obtained by the simple Guinier analysis and the overall description of the observed NPs, a more complex 2D simulation was performed and is presented in Fig. 10. The scattered intensity of densely packed particles represents a convolution of the form factor and the structure factor and is defined as the sum over the single contributions. In order to account for the scattering of the particles whose special positions are correlated we used the locally mono-disperse approximation (LMA), assuming that each individual particle is surrounded by particles of the same size [27]. The layered (vertical) structure factor is calculated allowing the layer thickness to vary randomly in a certain range, while the overall number of layers was varied too, simulating the vertical correlation length. The refraction effects at small grazing angles in GISAXS imposed the treatment of the scattering in the distorted-wave Born approximation [26].

Fig. 10 Shows the measured GISAXS intensity pattern (left half of

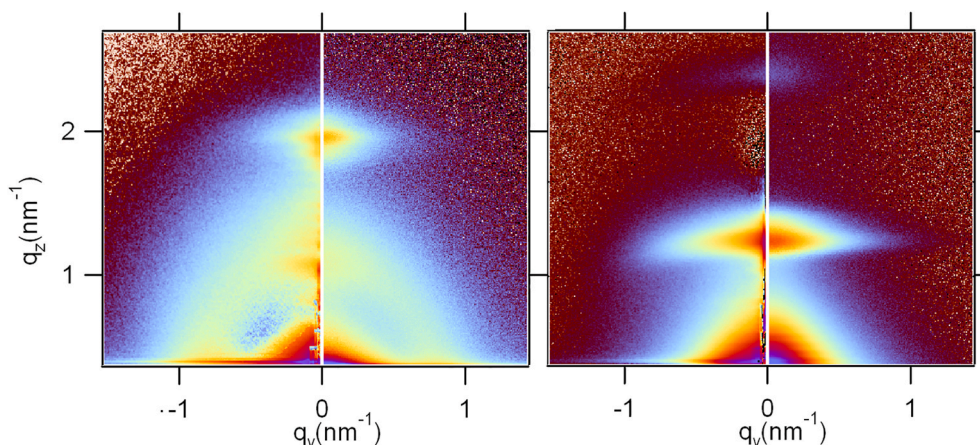


Fig. 10. GISAXS patterns of samples annealed at 525 °C (left) and at 550 °C in flowing N₂ atmosphere (right). Left column: as measured; right column: after subtraction of the surface scattering contribution taken at $\alpha = \alpha_c$.

each panel) and the obtained best simulation pattern (right half of each panel). In this simulation model the grown NPs are placed at the position of the continuous amorphous Ge layers, preserving thus the multilayer structure. However, they are not perfectly centered in each layer, but scattered narrowly around their center. To execute the simulation, the values of the NPs size obtained from the Guinier analysis shown in Fig. 6 and Table 2 were adopted as a starting point, as well as the inter-particle distance obtained from Fig. 7.

We found that the variation in the bilayer thickness was about 0.5 nm for both the A and B samples, while the thickness was 4.2 nm and 5.8 nm, respectively. The vertical correlation was about 18 bilayers for both samples, although the thickness itself was significantly different.

The form factor used in the simulation of the A2 sample was that of a 1.7 nm radius sphere, and the LMA structure factor contribution accounted for the ring like scattering. Additional, there is a smaller contribution from flat particles (with 1.7 nm and 4.0 nm vertical and horizontal elliptical semi-axis, respectively) [7].

As suggested by the Guinier analysis, the B2 sample lacks the LMA contribution, and it has a two-fold form factor: spherical particles with radius of 2.1 nm and flat (oblate) particles with radii 2.1 nm and 5.5 nm in vertical and horizontal direction, respectively.

The fit results shown in Fig. 10 are in very good agreement with the experimentally measured pattern, confirming therefore the parameters used in the NPs modelling.

3.4. Raman analysis

We applied also Raman spectroscopy to support our findings. Fig. 11 shows the results of Raman scattering on as-deposited samples, and the samples annealed at different temperatures where the onset of crystallization was observed by GIXRD. The characteristic fingerprint of the amorphous Ge layers is present with broad peaks close to 90, 190, 240 and 279 cm⁻¹ corresponding to the TA, LA, LO and TO (transversal and longitudinal acoustic and optical) modes, respectively [28]. After annealing at the onset of the crystallization temperature each type of sample (red and blue open symbols for the A2 and B2 samples, respectively) produced a sharp peak at 298 cm⁻¹ with a FWHM of 7.5 cm⁻¹, which is significantly broadened on the low frequency side in comparison to that of bulk Ge [29,30].

The Raman scattering therefore confirmed the GIXRD finding that the onset of the Ge QDs crystallization starts at 525 °C and 550 °C, at a much lower temperature than when multilayers were formed by magnetron co-sputtering of Ge and SiO₂ (where crystallization was reported at about 600 °C or above) [24,25,31]. The asymmetric profile of the peak (shoulder on the lower frequency side) can be often ascribed to the presence of very small crystallites [32]. In the fit we deconvoluted

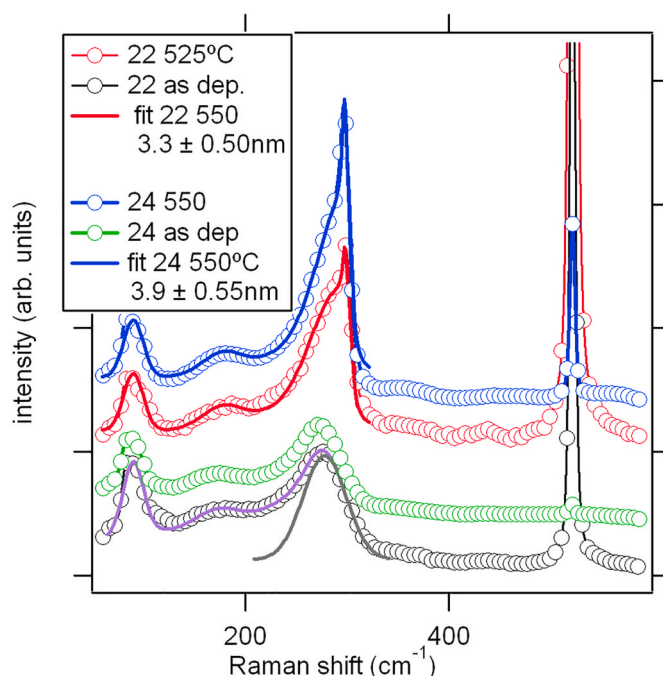


Fig. 11. Raman spectra (open symbols) of: as deposited (A1 black and B1 green), the A2 annealed at 525 °C (red), and B2 (at 550 °C, blue). The best fits are given as full line (see the text for details), indicating the formation of Ge-nanocrystals. (As the deposited film is semi-transparent to the used laser wavelength, the Si TO peak at 521 cm⁻¹ originating from the Si substrate is present with varying intensity in a function of the varying film structure.)

the observed peak close to 300 cm⁻¹ for both samples into three components. One (Lorentzian), due to the fully developed larger (though nanosized) crystalline Ge particles, at 298 cm⁻¹, one (Gaussian) due to the amorphous Ge component, at 279 cm⁻¹, and the remaining asymmetric component describing the smaller nano-Ge contribution [7]. Applying the analysis described in Refs. [7,33], the obtained nanoparticle size is $L \sim 3.3 \pm 0.50$ nm and 3.9 ± 0.55 nm for the A2 and B2 samples respectively, in good agreement with our GIXRD results discussed before. Moreover, from the integral intensities of the crystalline and amorphous peaks we obtained roughly a 50–60% crystallinity in both cases.

4. Discussion

Aiming to explore the possibility of growing Ge crystalline NPs with sizes in the 1–5 nm range we deposited and annealed multiple very thin (2 and 4 nm) amorphous Ge layers embedded between amorphous SiO₂ layers. GIXRD analysis revealed that for both multilayer systems the onset of the crystallization temperature is much lower than the earlier reported one [10], i.e. 525 °C and 550 °C for 2 nm and 4 nm thick Ge layer, respectively. Interestingly, it is shown that Ge crystallized partly after annealing, and regardless the difference in thickness, the crystallinity ratio reached about 50% in both multilayer cases.

The details of the surface morphology were analyzed by SEM and AFM microscopy. A good quality of the deposition process reflects in the rather smooth initial surface (as-deposited samples). Further an annealing process even more flattened the surfaces and thus supports a higher compactness of the deposited layers. A TEM study performed in the cross-section (X-TEM) mode showed a good stacking of the SiO₂/Ge layers, which are amorphous when deposited. Further annealing at given temperatures caused Ge NPs formation and partial crystallization (as shown by SAED analysis in Fig. 3).

The crystalline domains in the A2 sample (as revealed by GIXRD) were nearly spherical (as the measured dimensions in the <111>, <220> and <311> directions were nearly the same) and about 2 nm in diameter, while in the thicker 2/4 films (B2 sample) more oblate NPs formed with an average diameter of about 3 nm.

Raman analysis on the same samples showed that during annealing at the onset temperature of Ge crystallization the Raman peak due to the Ge–Ge vibration of the crystalline phase gave rise to a crystalline phase peak close to 300 cm⁻¹. The numerical deconvolution of this broad peak is in a very good qualitative agreement with both the Ge NPs size and crystallinity ratio, as compared to the GIXRD analysis. In spite of close contact of the amorphous Ge with the SiO₂ layers, the thermal treatment process did not induce SiGe alloying in measurable quantity, as no peak appeared close to 400 cm⁻¹, which is where the Si–Ge vibration mode is placed [34,35]. A complete lack of any Raman Si–Ge signal, along with SAED analysis, supports this conclusion.

Moreover, the absence of a peak close to 440 cm⁻¹ indicated that GeO₂ was not formed either [36], e.g. as a possible Ge core and GeO₂ thick shell. This however, does not exclude the possibility of thin oxide layer formation around the Ge NPs, as we shall see later on.

While GIXRD and Raman spectroscopy provided information on the size of the crystalline objects (domains), GISAXS complemented this information with the size, shape and interspacing of the objects that have an electronic density different from the matrix. As shown, NPs have grown in different sizes, as a function of the starting Ge layer thickness.

Samples with 2 nm thick Ge layers after the onset of crystallization at 525 °C produced almost spherical crystalline NPs. However, almost 50% of the original Ge layer remained amorphous. It is unclear whether the remaining amorphous phase exists as a separate isolated domain or if a core (crystalline)/shell (amorphous) structure is formed on a macroscopic scale.

Already in untreated Ge layers the clear maxima shown in Fig. 7., indicated the existence of evenly separated nuclei (at about 4.2 nm distance) in the amorphous phase, and the correlation distance increased to 7.2 nm after annealing. The simulation gave roughly the same numbers (see Table 2.). The Porod coefficient for the NPs formed by annealing is 3.6, which is less than the one for smooth NP surfaces (where it is 4), but bigger than for very rough NP surfaces (where it is 3).

However, when the thicker 4 nm Ge layers were annealed the onset of crystallization was at 550 °C. Also in this case annealing crystallized about 50% of the initially amorphous Ge layer. The reason for a rather large part of remaining amorphous Ge phase is the low annealing temperature and/or annealing duration, which will be further explored.

These thicker layers produced two kinds of crystallized NPs, smaller spherical ones of size 2.2 nm and bigger oblate spheroids with vertical axis of 2.3 nm and horizontal axis of 6.2 nm. The calculated Porod

coefficient for the formed NPs is 3.6 again, suggesting that the average surface roughness was about the same for both types of NPs. Furthermore, a detailed analysis of the Porod tail (presented in Fig. 8.) confirmed this findings, suggesting the existence of a 0.3–0.4 nm thick NP-to-matrix interface layer for both annealed samples.

5. Conclusion

We used e-gun assisted PVD deposition from solid sources in high vacuum to deposit multilayers consisting of alternating amorphous Ge (2 or 4 nm thick) and SiO₂ (2 nm thick) layers, aiming at annealing induced formation of crystalline Ge NPs of 1–5 nm in size, that are suitable for photovoltaics application.

SEM and AFM analysis showed a rather smooth surfaces formation after deposition, which were further flattened during the annealing.

The onset of crystallization occurred at 525 °C and 550 °C, respectively, even though about 50% of Ge remained amorphous after the annealing (for 1 h), as confirmed by GIXRD and Raman spectroscopy, as well as by X-TEM and SAED analysis. Additional macroscopic information (statistically relevant) was produced by a detailed GISAXS analysis. A careful simulation of the GISAXS pattern shows that thinner Ge layer clustered mostly into spherical NPs, while the thicker one produced a bimodal distribution consisting of smaller sphere-like NPs and larger oblate spheroids. The calculated simulations nicely fit the obtained experimental pattern. However, it remains unclear whether the remaining amorphous phase exists as a separate isolated domain or if a core (crystalline)/shell (amorphous) structure is formed on a macroscopic scale.

Declaration of competing interest

The authors declare that they have no known competing financial interests or personal relationships that could have appeared to influence the work reported in this paper.

Acknowledgments

This work has been supported in part by the Croatian Science Foundation under the project 6135. The support from CREST Center, North Carolina Central University, Durham, NC, USA, is also appreciated. JZ acknowledges the support by European Union's Horizon 2020 research and innovation programs under grant agreement No 823717 –ESTEEM3.

References

- [1] L. Pavesi, L. Dal Negro, C. Mazzoleni, G. Franzo, F. Priolo, *Nature* 408 (2000) 440–444.
- [2] S. Godfroy, M. Hayne, M. Jivanescu, A. Stesmans, M. Zacharias, O.I. Lebedev, G. Van Tendeloo, V.V. Moshchalkov, *Nat. Nanotechnol.* 3 (2008) 174–178.
- [3] F. Priolo, T. Gregorkiewicz, M. Galli, T.F. Krauss, *Nat. Nanotechnol.* 9 (2014) 19–32.
- [4] S. Mirabella, R. Agosta, G. Franzò, I. Crupi, M. Miritello, R. Lo Savio, M.A. Di Stefano, S. Di Marco, F. Simone, A. Terrasi, *J. Appl. Phys.* 106 (2009) 103505.
- [5] C. Bostedt, T. van Buuren, T.M. Willey, N. Franco, L.J. Terminello, C. Heske, T. Moeller, *Appl. Phys. Lett.* 84 (2004) 4056–4058.
- [6] B. Pivac, P. Dubcek, I. Capan, H. Zorc, S. Bernstorff, S. Duguay, A. Slaoui, *Thin Solid Films* 516 (2008) 6796–6799.
- [7] B. Pivac, P. Dubcek, J. Dasovic, H. Zorc, S. Bernstorff, J. Zavasnik, M.H. Wu, B. Vlahovic, *Vacuum* 179 (2020) 109508.
- [8] I. Honma, H. Hotta, H. Komiyama, K. Tanaka, *J. Non-Cryst. Solids* 97&98 (1987) 947–950.
- [9] G.V.M. Williams, A. Bittar, H.J. Trodahl, *J. Appl. Phys.* 67 (1990) 1874–1878.
- [10] G. Garcia, A.F. Lopeandia, A. Bernardi, M.I. Alonso, A.R. Goni, J.L. Labar, J. Rodriguez-Viejo, *J. Nanosci. Nanotechnol.* 9 (2009), 3031–3019.
- [11] (a) G.V.M. Williams, A. Bittar, H.J. Trodahl, *J. Appl. Phys.* 67 (1990) 1874–1878; (b) G. Garcia, A.F. Lopeandia, A. Bernardi, M.I. Alonso, A.R. Goni, J.L. Labar, J. Rodriguez-Viejo, *J. Nanosci. Nanotechnol.* 9 (2009), 3031–3019.
- [12] G. Radnoczi, B. Pecz, *Thin Solid Films* 232 (1993) 68–72.
- [13] A. Sestan, P. Jenus, S. Novak Krmpotic, j. Zavasnik, M. Ceh, *Mater. Char.* 138 (2018) 308–314.
- [14] H. Amenitsch, S. Bernstorff, P. Laggner, *Rev. Sci. Instrum.* 66 (1995) 1624–1626.

- [15] X.C. Wu, Ch Ossadnik, Ch Eggs, S. Veprek, J. Vac. Sci. Technol. B 20 (2002) 1368.
- [16] J.I. Langford, A.J.C. Wilson, J. Appl. Crystallogr. 11 (1978) 102.
- [17] A. Naudon, D. Thiaudiere, J. Appl. Crystallogr. 30 (1997) 822–827.
- [18] B. Pivac, P. Dubcek, J. Dasovic, H. Zorc, S. Bernstorff, J. Zavasnik, B. Vlahovic, J. Nanomater. (2018), 9326408.
- [19] G. Renaud, R. Lazzari, F. Leroy, Surf. Sci. Rep. 64 (2009) 255–380.
- [20] B. Pivac, P. Dubček, I. Capan, H. Zorc, J. Dasović, S. Bernstorff, M. Wu, B. Vlahovic, Phys. Status Solidi 210 (2013) 755–759.
- [21] M. Störmer, J.-M. Andre, C. Michaelsen, R. Benbalagh, P. Jonnard, J. Phys. D Appl. Phys. 40 (2007) 4253–4258.
- [22] B. Hammouda, J. Appl. Crystallogr. 43 (2010) 716–719.
- [23] J.S. Pedersen, J. Appl. Crystallogr. 27 (1994) 595–608.
- [24] B. Pivac, P. Dubcek, J. Popovic, J. Dasovic, S. Bernstorff, N. Radic, J. Zavasnik, J. Appl. Crystallogr. 49 (2016) 1957–1966.
- [25] Branko Pivac, Pavo Dubček, Jasna Dasović, Jasminka Popović, Nikola Radic, Inorg. Inside Chem. 57 (2018) 14939.
- [26] S.K. Sinha, E.B. Sirota, S. Garoff, H.B. Stanley, Phys. Rev. B 38 (1988) 2297.
- [27] J.S.J. Pedersen, Appl. Cryst. 27 (1994) 595.
- [28] Y. Sasaki, C. Horie, Phys. Rev. B 47 (1993) 3811.
- [29] J. Parker Jr., D.W. Feldman, M. Ashkin, Phys. Rev. 155 (1967) 712–714.
- [30] A.V. Kolobov, J. Appl. Phys. 87 (2000) 2926–2930.
- [31] J. Dasovic, P. Dubcek, I. Pucic, S. Bernstorff, N. Radic, B. Pivac, Appl. Surf. Sci. 414 (2017) 1–7.
- [32] E. Bustarret, M.A. Hachiha, M. Brunel, Appl. Phys. Lett. 52 (1988) 1675–1677.
- [33] Z. Hao, S.A. Kochubei, A.A. Popov, V.A. Volodin, Solid State Commun. 313 (2020) 113897.
- [34] M.I. Alonso, K. Winer, Phys. Rev. B39 (1989) 10056–10060.
- [35] A.A. Shklyayev, V.A. Volodin, M. Stoffel, H. Rinnert, M. Vergnat, J. Appl. Phys. 123 (2018), 015304.
- [36] P.K. Giri, S. Dhara, J. Nanomater. 2012 (2012), 9051.